Characterizing the Formation of Organic Layers on the Surface of Inorganic/Aqueous Aerosols by Raman Spectroscopy

Jariya Buajarern, Laura Mitchem, and Jonathan P. Reid*

School of Chemistry, University of Bristol, Bristol BS8 1TS, U.K.

Received: June 27, 2007; In Final Form: August 31, 2007

We demonstrate that nonlinear Raman spectroscopy coupled with aerosol optical tweezers can be used to probe the evolving phase partitioning in mixed organic/inorganic/aqueous aerosol droplets that adopt a core−shell structure in which the aqueous phase is coated in an organic layer. Specifically, we demonstrate that the characteristic fingerprint of wavelengths at which stimulated Raman scattering is observed can be used to assess the phase behavior of multiphase decane/aqueous sodium chloride droplets. Decane is observed to form a layer on the surface of the core aqueous droplet, and from the spectroscopic signature the aqueous core size can be determined with nanometer accuracy and the thickness of the decane layer with an accuracy of ±8 nm. Further, the presence of the organic layer is observed to reduce the rate at which water evaporates from the core of the droplet with an increasing rate of evaporation observed with diminishing layer thickness.

I. Introduction

It is now widely recognized that surface active organic components play an important role in governing the properties of atmospheric aerosol, influencing rates of heterogeneous chemistry, modifying cloud droplet microphysics, and affecting mass transfer rates between the gas and condensed phases.[1−7] Biogenic fatty acids with carbon chain lengths of 14−18 units, such as palmitic acid, have been identified as being primary constituents in organic surface coatings of marine aerosol.[8,9] Longer carbon chain length fatty acids have been identified on continental sulfate aerosol, with the primary source of the organic component attributed to the burning of terrestrial biomass.[10] Further, it is expected that the surface activity of a wide variety of organic compounds present in the atmosphere is likely to lead to the formation of mixed films exhibiting distinctive behavior reflecting the complex interactions between the different components. Gilman et al. have suggested that the mixed films formed by simple long chain hydrocarbons and fatty acids can provide a valuable proxy for considering the properties of organic films on atmospheric aerosol.[11] Further, the condensation of organic components onto an aerosol particle can lead to formation of thick layers and may not be limited to the presence of a monomolecular film.[12]

Not only is it essential to characterize the composition of mixed organic films on atmospheric aerosol but it is important to understand the influence of organic films on the kinetics of reactive uptake of trace gas species and the uptake of water.[12−14] It has been suggested that the presence of an organic layer may lead to a reduction in mass accommodation coefficients and a reduction in the mass transfer rate. An aerosol particle that is fully coated with an organic film may present a hydrophobic surface to accommodating water molecules and inhibit mass transfer.[7] This has been referred to as an inverted micelle model.[15] Further, when thick coatings of an organic film are present, the impact of the solubility and the diffusion rate of the accommodating species within the organic phase must be considered.[12]

In previous work we have demonstrated that a single-beam gradient-force optical trap (optical tweezers) can be used to capture and retain a single aerosol droplet for an indefinite period of time.[16] The formation of multiple optical traps in parallel can allow the independent manipulation of multiple aerosol particles, permitting studies of coagulation and accurate measurements of relative humidity (RH).[17,18] A Raman signature from the trapped droplet provides information on the composition, size, and refractive index of the droplet, allowing investigations of the response of equilibrium particle size to changes in RH.[18] Further, we have demonstrated that such an approach can be used to investigate the properties of a mixed phase droplet containing phase segregated organic and aqueous domains. Images recorded by conventional brightfield microscopy of the trapped droplet allow the separation of phases to be confirmed; spontaneous Raman scattering allows the composition to be interrogated with spatial resolution.[19,20]

In this publication we present a strategy for examining the impact of organic films on the properties of aerosol, focusing in particular on studies of single aqueous sodium chloride droplets coated with a volatile organic surface film, in this case *n*-decane, referred to subsequently as decane. Specifically, we will demonstrate that nonlinear stimulated Raman scattering (SRS) can enable the interrogation of organic films on the surface of an aqueous droplet with high time resolution, allowing the determination of film thickness with nanometer accuracy. The advantages of combining this approach with optical tweezers include the option to periodically dose the trapped droplet with different organic components through controlled coagulation and the ability to characterize the trapped droplet through conventional brightfield microscopy. In the following section we describe the experimental technique before considering the Raman spectroscopy of core−shell structured droplets in Section III. Section III.a examines the theoretical basis for the measurements and presents the method used to analyze the Raman spectra. In Sections III.b and III.c we contrast the Raman spectroscopic signatures arising from aqueous droplets with those observed from aqueous droplets coated with thin (<100 nm) or thick (>500 nm) organic layers.

10.1021/jp075021v CCC: $37.00
Published on Web 10/25/2007

II. Experimental Technique

The aerosol tweezing measurements have been performed on two different instruments, both of which have been described in detail in previous publications.[16,17,20] The first instrument is based around a commercial Leica DM IRB microscope. An Ar-ion laser operating at 514.5 nm is used to form the optical trap and provide the excitation wavelength for the spectroscopic measurements. The second instrument is based around a custom-designed inverted microscope design and employs a Nd:YVO_4 laser (Coherent VERDI V5) operating at 532 nm. In the former case, the optical trap is formed by focusing the laser light through a 60× oil immersion objective, while a 100× objective is used for the custom-designed system. Formation of the optical trap with radiation in the green region of the electromagnetic spectrum minimizes droplet heating with the complex refractive index of water being less than 10^{-8} in this region.[16]

Images of the trapped droplets are acquired by conventional brightfield microscopy. Backscattered Raman light is collected by the microscope objective and analyzed using a 0.5 m spectrograph (Spectra Pro 2500i Acton Research Corporation), equipped with a diffraction grating (1200 g/mm) and coupled to a CCD camera (Princeton Instruments). The Raman spectra are acquired with a typical spectral dispersion of 0.03 nm/pixel. Any unwanted elastic scatter from the laser is eliminated by an edge filter. Raman spectra are typically acquired using 1 s time integration, unless otherwise stated.

Aqueous aerosol is generated using an Omron NE-U07 medical nebulizer and all solutions used in this work contain 0.34 M sodium chloride. The presence of sodium chloride lowers the vapor pressure of the droplet, allowing the droplet to be retained indefinitely in the optical trap under conditions of subsaturation.[16] The organic aerosol, ethanol and decane, is also generated with an ultrasonic nebulizer. In most of the measurements presented here, an aqueous droplet is first loaded into the optical trap and it is then bombarded with organic aerosol droplets. Prolonged dosing increases the volume of organic component mixed with the aqueous phase. The gas phase humidity can be controlled by the introduction of a flow of humidified nitrogen into the aerosol cell. Although there is no active temperature control of the experimental apparatus, the laboratory is temperature stabilized with typical temperature fluctuations of <1 K over a 1 h period.

III. Raman Scattering Measurements of Evaporating Core−Shell Organic/Aqueous Droplets

We first examine the nonlinear stimulated Raman scattering (SRS) signature expected from layered microdroplets with a core−shell structure, consisting of a shell of higher refractive index than the droplet core. We then explore the mixing state of ethanol and aqueous components in a multicomponent droplet before investigating the phase partitioning of decane and water in a biphase droplet.

III.a. Theoretical Considerations. Raman spectroscopy can be used to characterize the composition, size, and refractive index of an optically tweezed droplet. The concentration of Raman active species can be determined from a comparison of the spontaneous Raman scattering intensity arising from a droplet with calibration measurements.[21] The size of a droplet can be determined with nanometer accuracy by examining the unique spectroscopic fingerprint of the resonant structure arising from SRS.[21] Raman fingerprints from three droplets are compared in Figure 1. Although the droplets are of similar size (∼4 μm radius), they consist of different phase separated structures: a homogeneous aqueous droplet, a droplet with an aqueous core and a thin 10 nm organic film, and a droplet with a reduced aqueous core and a thick 600 nm organic shell. These three spectral signatures are now compared in order to illustrate the impact of inhomogenieties in refractive index on the spectroscopic signature.

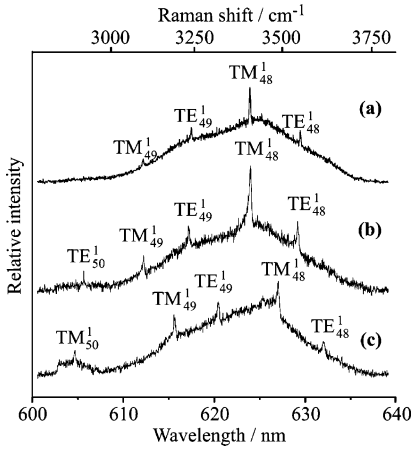

Figure 1. Raman spectra obtained from (a) a 4.04 μm radius aqueous sodium chloride droplet, (b) a 3.99 μm radius aqueous droplet coated with a 0.01 μm decane shell, and (c) a 3.37 μm radius aqueous droplet coated with a 0.60 μm decane shell.

The Raman scattering spectrum recorded from a droplet consists of an underlying continuous band arising from spontaneous Raman scattering. In each of the Raman signatures presented in Figure 1, the O−H stretching vibrations of water molecules present within the droplet are excited at a Stokes shift of greater than 3000 cm^{-1}.[22−25] In addition, excitation of the C−H stretching vibrations at wavelengths centered around 605 nm (∼2900 cm^{-1} Raman shift) is apparent in the Raman signature for the droplet consisting of a thick decane shell surrounding an aqueous core, Figure 1c. SRS appears at wavelengths commensurate with whispering gallery modes (WGMs) and is superimposed on the spontaneous band.[19,26] At these wavelengths, the droplet behaves as a low loss optical cavity, and the Raman intensity builds to a level at which the threshold intensity for SRS is surpassed. By comparison with Mie scattering calculations, the WGMs can be assigned a mode number that defines the number of wavelengths of light forming a standing wave around the circumference of the droplet. Further, each mode can be assigned a mode order, which defines the number of maxima in the intensity of the light in the radial coordinate. A mode with no radial dependence in the electric field is referred to as a transverse electric mode (TE), and one exhibiting no dependence in the magnetic field as a transverse magnetic mode (TM). The mode number and mode order are specified as subscripts and superscripts, respectively, following the indication of the mode polarization, TE or TM.

Although the resonant structure appears in all three spectra shown in Figure 1, the relative pattern in the alternation of TE and TM modes differs with the TE mode shifting closer in wavelength to the TM mode of shorter wavelength for spectra b and c when compared to a. This is most apparent when comparing a and b for which the TM modes occur at similar wavelengths. Such a change in the pattern of modes provides a signature of a core−shell droplet in which the droplet core and shell have different refractive indices. The terms layer and shell are used interchangeably. Further, the resonant modes have a larger width in b and c and show a degree of asymmetry, with a shading toward shorter wavelength. Nonuniformity of the surface layer could lead to such asymmetry, and this will be discussed in further detail later.

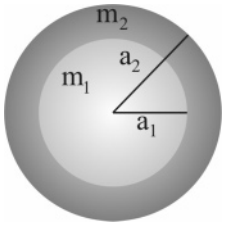

Figure 2. Definition of the core and total radii and refractive indices for a core−shell structured droplet.

Aden and Kerker were the first to consider an accurate formulation of Mie scattering by concentrically layered spheres.[27] Toon and Ackerman provided an accurate reformulation of the problem that allowed numerically stable calculations of the light-scattering intensity for particles with cores and shells of any relative size.[28] Measurements by Ray and co-workers[26,29,30] examined layered spheres experimentally by recording the elastic light scattering intensity as a function of illuminating wavelength using a ring dye laser as the tunable wavelength source. A Santovac 5 (polyphenol ether) droplet was exposed to a gas stream of Fromblin (perfluorinated polyether), two components that are almost completely immiscible, generating a layered droplet. In measurements that examined the evaporation of the layer, the layer was observed to evaporate from 38.5 nm thick to about 15 nm over 10000 s, and the authors reported measurements of thickness changes as small as 0.5 nm.

A key difference between the experiments presented here and previous work is that measurements are performed with high time resolution on droplets containing two volatile components, decane and water. Further, measurements of a range of WGMs of varying polarization, order, and number are made simultaneously by recording an entire inelastic scattering Raman band with the spectrograph/CCD, rather than identifying when the droplet is on-resonance with a single wavelength through elastic scattering measurements. An important parameter to note at this point is that the dispersion per pixel on the CCD chip using a 1200 g/mm grating is 0.03 nm. This primarily determines the accuracy with which film thicknesses and droplet sizes can be recorded. Simultaneous measurements of spontaneous Raman scattering alongside the WGM fingerprint allow the change in size, layer thickness, and composition to be probed in a single measurement with high time resolution.

Figure 2 illustrates the structure of a core−shell droplet. The core of the droplet has a refractive index m_1 and radius a_1, and the shell has a refractive index m_2 with an outer radius a_2. In this publication, Mie scattering calculations for a core−shell droplet were performed using an adapted version of the coated-sphere code developed by Wiscombe.[31] The refractive index of aqueous sodium chloride is assumed to follow the concentration and wavelength dependence described in reference 36, and the refractive index of decane is assumed to be 1.411 at 650 nm.[32] Calculations and measurements for multicomponent ethanol/aqueous sodium chloride droplets are compared with those for decane/aqueous sodium chloride droplets. While in the latter case the measurements should be characterized by layer formation due to the immiscibility of decane and water, in the former case spectral signatures should correspond to those for a homogeneous droplet.[33] The refractive index of pure ethanol was assumed to be 1.361, while the wavelength and compositional dependent refractive index of ethanol/water/sodium chloride solutions was taken to be that described in reference 36.

In Figure 3 we compare predictions of the WGM wavelengths appearing on the O−H Raman band for a homogeneous aqueous sodium chloride droplet and a core−shell aqueous sodium chloride/decane droplet. In both cases the first simulation is for an aqueous sodium chloride droplet (0.34 M) of radius 3.0 μm. Calculations for the homogeneous aqueous droplet examine the change in WGM wavelengths with an increase in droplet size through growth in the aqueous phase, Figure 3a. In the core−shell case, the additional size is gained solely from increasing the thickness of a decane shell on the 3.0 μm aqueous core, Figure 3b. Thus, calculations at a radius of 3.5 μm correspond to a droplet with an aqueous core of 3.0 μm and a decane shell thickness of 500 nm. Although for the homogeneous droplet the TE and TM modes shift by similar wavelengths with increasing size, it is evident that the TE and TM modes show a different sensitivity to size change in the core−shell case. This difference in sensitivity is highlighted by the different gradients of the wavelength dependencies shown in Figure 3 and is consistent with the observations described in Figure 1.

A convenient method for examining the shifting pattern of TE and TM modes is to calculate the mode offset, reflecting the wavelength of a TM mode in relation to the two neighboring TE modes of the same order and consecutive mode number. The mode offset is defined as the magnitude of the difference between the TE−TM spacing to shorter wavelength and the TE−TM spacing to longer wavelength. When the TM mode is situated exactly at the midpoint between the surrounding TE modes, the mode offset is zero. The mode offset allows a first assessment of the degree of homogeneity of a droplet to be made.

In Figure 4, the variation in mode offset with change in decane layer thickness is compared for droplets with an aqueous sodium chloride core of radius 3 and 5 μm. The simulations for the core−shell droplet are also compared with those for homogeneous spheres of aqueous sodium chloride and decane of a total size determined by the sum of the core and shell, Figure 4a. For a core of radius 3 μm, the maximum in mode offset occurs at a shell thickness of 0.2 μm, at which point the TM modes are aligned with the TE modes. Although it is clear that the mode offset cannot be used to definitively give the shell thickness, a full Mie scattering fit is able to provide an accurate estimation of the core and shell sizes as the overall spacing of modes of the same polarization changes slightly with total droplet size. The mode offset is initially close to that for a homogeneous aqueous droplet, tending to that for a pure decane droplet in the limit of a thick shell. This is in agreement with previous observations: when a layer is thicker than 20% of the droplet radius, the WGMs from the layered and homogeneous sphere of the shell refractive index are indistinguishable.[26] The light intensity is concentrated within the shell with little propagation to the depths required to penetrate to the core. The penetration depth of a WGM in a homogeneous sphere can be estimated from the expression $a(1-1/m)$, where a is the droplet radius and m is the refractive index.[21,34] Thus, for a decane droplet 4 μm in diameter the WGM penetrates to a depth of $\sim$1.2 μm.

In the case of the 5 μm droplet core, second-order modes must also be considered, for which the internal field penetrates deeper into the droplet than for first-order modes. Although the second-order modes are less sensitive to thin shells, significant deviations in the mode offset are observed for layer thicknesses greater than 0.6 μm. For layer thicknesses approaching $\sim$1.2 μm, the mode offset again becomes insensitive to a further increase of layer thickness and tends to that for a homogeneous decane droplet. The trends in mode offset reported in Figure 4 provide a method for reducing the search space for iteration

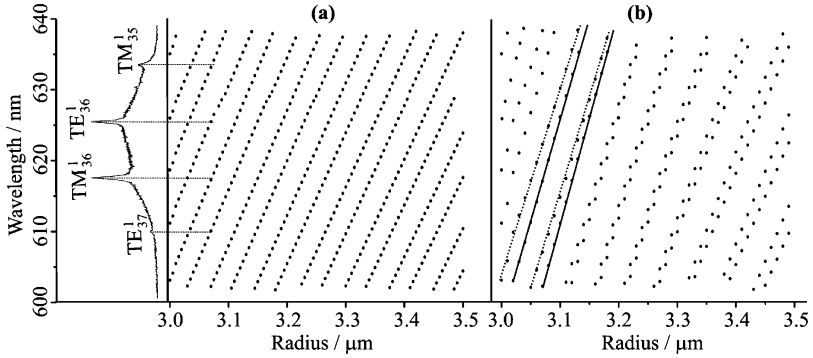

Figure 3. Simulation of the WGM wavelengths for (a) an homogeneous aqueous sodium chloride droplet increasing in size from 3.00 to 3.50 μm radius (an experimental spectrum for an aqueous droplet of 3.07 μm radius is shown for comparison) and (b) an aqueous sodium chloride droplet of 3.00 μm radius coated with a decane film of increasing thickness giving the total droplet radius as indicated. The calculations are performed at the discrete sizes shown by the dots, and the difference in gradients of the shifting of TE and TM modes is indicated in panel b.

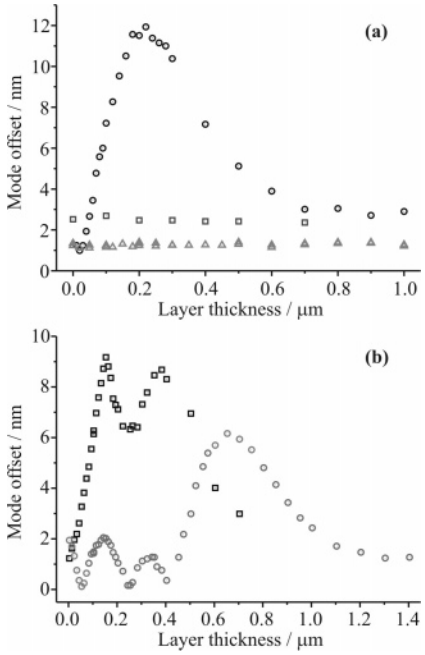

Figure 4. (a) Change in mode offset for first-order modes for an aqueous sodium chloride droplet (core radius of 3 μm) coated in a decane film of increasing thickness (circles). The mode offset of homogeneous aqueous droplets (triangles) and pure decane droplets (squares) of increasing radius are shown for comparison. (b) Change in mode offset for first- (squares) and second- (circles) order modes for a 5 μm radius aqueous sodium chloride droplet core coated in a shell of decane of increasing thickness.

over core and shell size in the analysis of the spectral fingerprints. However, subsequent results apply a full Mie scattering fit to the experimental data.

We have so far considered a core−shell droplet formed from aqueous sodium chloride and decane phases of fixed composition and, thus, refractive index. It is instructive to consider at this stage the impact of uncertainties in the refractive indices of the core and shell on the determination of calculated best-fit core and shell radii. The dependence of the mode offset on the refractive index of the shell relative to the core is shown in Figure 5. The mode offset varies significantly with shell refractive index for a droplet with a 4 μm diameter core and a 100 nm thick shell. Given the insolubility of sodium chloride in decane and the low miscibility limit of water in decane with values between 1 to 3 $\times$ 10^{-4},[35] the uncertainty in the composition of the decane shell leads to an uncertainty in the refractive index of $\pm$0.0001. This is confirmed by bulk phase measurements of refractive index at 589 nm for which an identical value of 1.4126 was measured for samples of pure decane, a saturated solution of sodium chloride in decane, and the organic phase of a water/sodium chloride/decane solution. Thus, the uncertainty in refractive index is considered to be negligible and is ignored in the analysis presented below; the decane phase is assumed to have a constant refractive index during all measurements. Indeed, calculations show that an uncertainty in refractive index of $\pm$0.002, 20 times that considered to be reasonable here, leads to a fitting error in the shell thickness of $\pm$8 nm for a droplet with a 4 μm radius aqueous core and a 200 nm thick decane shell.

In Figure 5 calculations are also presented for two core refractive indices: an aqueous sodium chloride core of salt concentration 20 g/L (the starting concentration of salt considered here) and a more concentrated core of 100 g/L (considered as the highest limiting concentration possible in this work). In the analysis presented below, the refractive index of the aqueous core is assumed to be time dependent with the concentration of sodium chloride determined at all core sizes by the initial volume of the aqueous phase immediately following capture of the aqueous droplet. This procedure has been adopted in previous work.[37] Given the extremely low solubility of decane in water,[35] this is a robust method for treating the refractive index of the droplet core, and the errors in the core and shell size incurred are negligible (<1 nm).[37] The insensitivity of the mode offset to change in refractive index of the core (Figure 5) confirms that the determination of the shell thickness is not compromised by uncertainties in the core composition.

In order to establish the mixing state of the organic and aqueous components and determine the core and shell sizes for a layered droplet from an experimental spectrum, Mie scattering calculations were performed over a grid of core and shell sizes, with typical step sizes in core and shell radii of 5 nm, allowing the characteristic wavelengths of WGMs to be identified. The wavelengths of WGMs at intermediate core and shell radii were obtained by interpolation. Each experimental spectrum was compared with a particular calculated spectrum and the sum-of-squares difference between WGM wavelengths in the measured and simulated spectrum determined. This comparison was repeated for each simulated spectrum, allowing the calculated spectrum that most accurately represents each measured spectrum to be identified. This provides a final estimate of the best-fit core and shell radii for each spectrum. Such a method provides a computationally efficient method for modeling an experimental run that may contain many thousands of spectra, given that the time resolution typically used in this work is 1 s. Further, each spectrum is evaluated independently, providing a stringent assessment of the quality of the fit for each spectrum

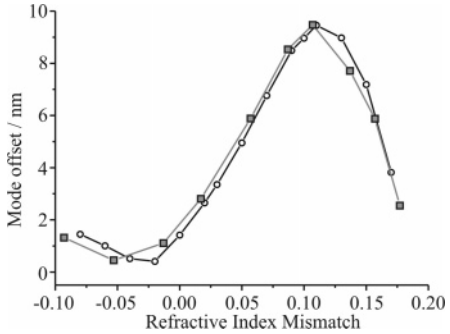

Figure 5. Dependence of the mode offset on the refractive index of the core and the shell. The refractive index mismatch is defined as the refractive index of the core subtracted from the refractive index of the shell. Thus, a negative refractive index mismatch corresponds to a shell of lower refractive index than that of the core and vice versa. The calculations are performed for a droplet consisting of an aqueous sodium chloride core of 4 μm radius (20 g/L salt concentration or 100 g/L, open black circles and filled gray squares, respectively) and a 100 nm thick shell of variable refractive index. For the aqueous sodium chloride/decane droplets considered here, the mismatch is ~0.08.

when compared to the overall experimental trend and a definitive assignment of the core−shell structure. Typical wavelength errors in reproducing the experimental resonant wavelengths for core−shell droplets are comparable to the spectral dispersion of the spectra or less (0.03 nm/pixel). When the fit is constrained to fit the spectrum to an homogeneous droplet, the error typically rises by an order of magnitude, depending on the thickness of the shell.

III.b. Probing the Internal Structure of Aqueous/Ethanol Droplets Formed on Coagulation. We first consider the coagulation of an aqueous sodium chloride droplet with an ethanol droplet. In this case, the organic and aqueous components are expected to be fully miscible. Although the surface may exhibit an excess of ethanol,[38] no discrete step in refractive index is anticipated between a core and shell of different refractive index. In these measurements, an aqueous sodium chloride droplet was first loaded into the optical trap. The tweezed droplet was then bombarded with a flow of ethanol aerosol leading to discrete coagulation events and an increase in size and ethanol concentration. Following coagulation, a change in the pattern of WGMs was observed, as shown in Figure 6a, along with a change in the Raman intensity at shifts around 2900 cm^{-1}, corresponding to excitation of the C−H stretching vibrations of ethanol.[39,40] Over time, the ethanol vapor disperses from the cell, and ethanol evaporates from the droplet leading to a decrease in droplet size, reflected by a shift in resonant wavelengths to the blue. In addition, this is accompanied by a decrease in the concentration of ethanol reflected by a decrease in the CH spectral intensity. The droplet size (assuming miscibility and changing refractive index with composition) and the C−H to O−H intensity ratio show similar time dependencies and are reported in Figure 6b. The droplet volume decreases by a factor of 1.8 over 20 min, consistent with the change in C−H to O−H intensity ratio, which also declines by a factor of 1.8 ± 0.2 with a constant aqueous component.

At early times following coagulation, the mode offset was observed to remain constant at 1.40 ± 0.03 nm, showing no systematic variation with time as shown in Figure 7. For comparison, the mode offset would be 1.82 nm for a pure ethanol droplet (equivalent to assuming a thick layer of ethanol on the surface of the water droplet) and 1.26 nm for the initial aqueous sodium chloride droplet. This suggests that the ethanol and aqueous components must be well mixed on coagulation.

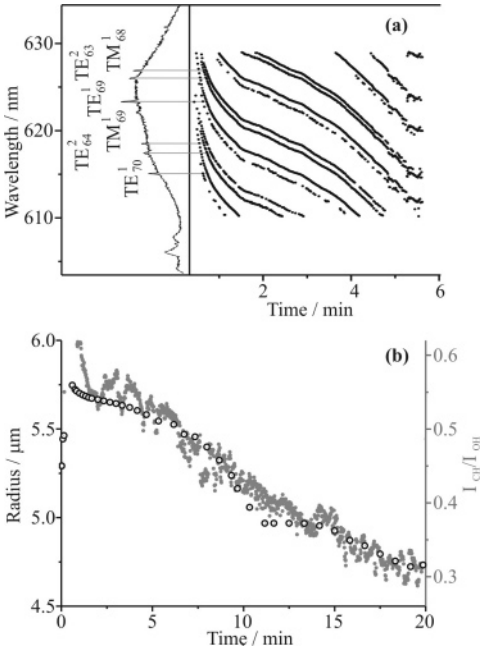

Figure 6. (a) The change in WGM wavelengths with time following coagulation and formation of an aqueous sodium chloride/ethanol droplet. (b) The time variation of the calculated droplet radius (open black circles, left axis) and the spontaneous Raman C−H to O−H band intensity ratio (filled gray circles, right axis) during droplet evaporation.

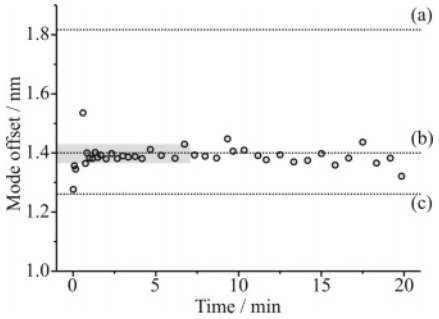

Figure 7. Variation in the mode offset of the experimental results for the aqueous sodium chloride/ethanol droplet considered in Figure 6a. The mode offset is compared with the mode offset obtained for (a) a pure ethanol droplet (5 μm), (b) a miscible ethanol/aqueous droplet (5 μm, 20% v/v ethanol), and (c) a pure sodium chloride aqueous droplet (5 μm). The gray area highlights the expected uncertainty in the wavelength determination arising from the spectral dispersion of 0.03 nm/pixel. There is a notable increase in the scatter and decline in the offset at long time as the proportion of ethanol in the droplet declines.

A mode offset of 1.40 nm is expected for an ethanol/aqueous sodium chloride droplet of the composition governed by the sodium chloride concentration in the nebulized solution and the droplet volume increase on addition of ethanol at coagulation. At long times, the scatter in the mode offset becomes more significant, and there is an apparent decline in the value as the proportion of ethanol in the droplet diminishes.

III.c. Probing the Internal Structure of Aqueous Sodium Chloride/Decane Droplets Formed on Coagulation. We now consider the coagulation between two immiscible droplets, aqueous sodium chloride and decane. An aqueous droplet is first trapped and then dosed with a flow of decane aerosol. In previous work we have shown that, following coagulation, SRS is quenched by significant inhomogeneities in composition and refractive index within the droplet and these inhomogeneities are apparent from the images recorded.[19] By considering the appropriate surface and interfacial tensions, the equilibrium structure of the mixed phase droplet can be predicted,[41] and

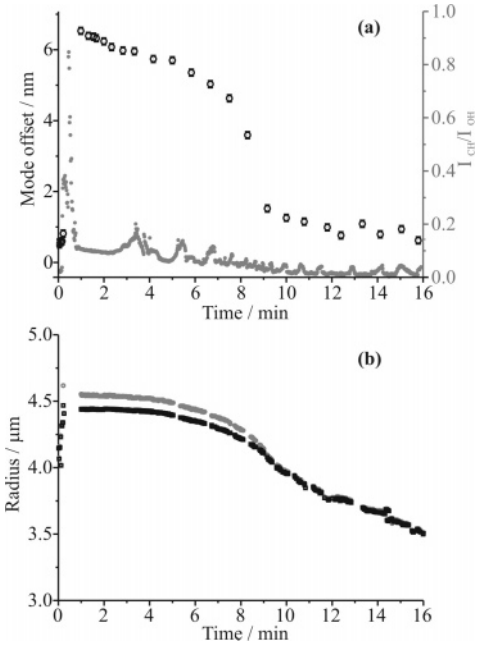

Figure 8. (a) The time dependent variation in mode offset of first-order modes (open black circles, left axis) and the corresponding C−H to O−H band intensity ratio (right axis, filled gray circles) following coagulation of an aqueous sodium chloride droplet with decane droplets. (b) The core (black) and total (gray) radii of the aqueous sodium chloride/decane droplet estimated from Mie scattering calculations for a core−shell droplet.

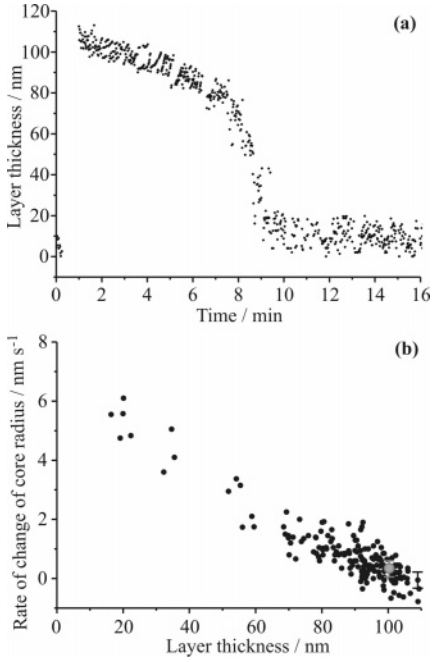

Figure 9. (a) The time dependence in the layer thickness of a decane layer on the aqueous droplet, calculated using Mie scattering calculations for a layered sphere. This is for the experiment presented in Figure 8. (b) Correlational plot for the rate of change in the droplet core radius over time with decane layer thickness. A typical error bar is shown for the point shown at largest layer thickness. The gray circle with error bar represents the gradient observed for evaporation of an aqueous core surrounded by a thick decane film of ∼550 nm presented in Figure 10b.

different degrees of engulfing of the aqueous sodium chloride/decane droplet are expected depending on the relative sizes of the two droplets of the different components undergoing coagulation. However, the volatility of the organic component leads to a phase distribution that varies with time. Once a significant fraction of the organic component has evaporated, usually a couple minutes after coagulation, the SRS is observed to once again surpass threshold and a single progression of modes extending over both the C−H and O−H stretching bands is observed. This suggests that residual decane remains within the aqueous droplet and occupies a volume probed by the light intensity of the WGMs.

Initially, once WGMs are apparent in the spectral fingerprint, the TE and TM modes are close in wavelength, corresponding to a large mode offset. Further, unequal shifts of the TE and TM modes are observed with time, suggesting the presence of a decane layer on the surface of the aqueous droplet. This is supported by an examination of the temporal variation in the mode offset, shown in Figure 8a, which increases to a value significantly larger than its value prior to coagulation once the WGMs reappear 1 min after coagulation. The offset then rapidly declines at a time of 8 min. In Figure 8a we also report the variation in the C−H to O−H Raman intensity ratio. Following coagulation, the C−H intensity is comparable to the O−H intensity. This is followed by a rapid decline over a period of ∼20 s as the organic component evaporates from the droplet and SRS once again surpasses threshold. At long times, the intensity of the C−H stretching vibration returns to close to the pre-coagulation value, consistent with the trend in the mode offset. Caution is required in interpreting the intensity ratio. The intensities of the C−H and O−H stretches are integrated in this analysis between wavelengths of 603−604 nm and 625−626 nm, respectively. As WGMs move through this integration window the C−H integrated intensity is enhanced, yielding occasional peaks in the integrated intensity ratio. This also serves to illustrate that even though the spontaneous C−H Raman scattering intensity returns to zero, decane remains in the droplet as it is observed in the SRS signal.

The time dependencies of the total droplet and core radii are reported in Figure 8b, estimated from full Mie scattering calculations for a core−shell droplet. In the period 5−10 min, the total droplet radius tends toward the droplet core radius, reflecting a decrease in the thickness of the decane shell. This is similarly reflected in the decline in the C−H integrated intensity in the SRS signal with time. After 10 min, the mode offset returns to a value close to the initial starting value for an aqueous sodium chloride droplet. The change in layer thickness is shown explicitly in Figure 9a, showing an abrupt decrease at times between 8 and 10 min. After 10 min the decane layer thickness is found to remain approximately constant at 10 ± 8 nm with this range providing a measure of the accuracy with which the film thickness can be determined. It should be noted that SRS from CH persists even to the longest times, suggesting that a decane film is retained on the droplet surface. The solubility limit of decane in water is 1.89×10^{-9}, considerably lower than the spontaneous Raman detection limit for decane.[35]

The time dependence of the core size and layer thickness suggests that the rate of evaporation of water is limited by the presence of the decane film. In Figure 9b, the correlation between the rate of size change of the core, an unambiguous measure of the evaporation rate of water from the droplet, with the layer thickness is examined. With increasing layer thickness, the rate of evaporation of the core diminishes. Indeed, the rate of decrease of the core size is initially very slow at times earlier than 7 min, but it rapidly increases when the layer thickness begins to diminish. Qualitatively such behavior is consistent with the low solubility of water in the organic component, which acts to suppress the mass transfer of water from the droplet core into the surrounding vapor.

Ray et al.[30] considered the evaporation of a volatile droplet core through an involatile coating. The interplay of two opposing factors was shown to determine the evaporation rate of the core. For a core species that is soluble in the shell and diffuses rapidly, an increasing shell thickness was found to increase the evaporation rate due to the increasing surface area for evaporation. However, for a less soluble species diffusing slowly through the shell, an increase in the shell thickness was found to lower the concentration of the evaporating component at the outer surface significantly, reducing the evaporation rate. The former effect was found to dominate in the evaporation of glycerol through a shell of involatile dioctyl phthalate (DOP), which showed an enhanced evaporation rate over that for a droplet of the core size. Measurements were made of evaporation rates into a gas environment devoid of glycerol vapor.

Although we have applied the model described by Ray et al.[30] to studies of water evaporation through decane films, a direct quantitative comparison is not at this stage feasible. The shell component is volatile, leading to a varying shell thickness with time, and the gas phase is not dry and contains water vapor. Measurements are required that can allow the unambiguous determination of the gas phase composition. However, the general trend is clear. Although the miscibility limits of glycerol in DOP and water in decane are similar,[30,35] with values around 1 to 3 $\times$ 10^{-4}, and the diffusion coefficients of water and glycerol in the two shell phases are likely to be similar,[12] water is considerably more volatile than glycerol, with vapor pressures of 2338 and 2.2 $\times$ 10^{-2} Pa, respectively.[30,32] This is the primary factor that leads to a decane film retarding the mass transfer rate of the aqueous core. In future studies we will use a second aqueous control droplet, trapped within a few 10s of micrometers from the core−shell droplet to probe the gas phase composition, specifically the partial pressure of water.[17] This will allow quantitative calculations to be performed and compared with theory.

Up to this point we have considered the formation of thin organic films, <100 nm in thickness, on aqueous droplet cores of less than 5 μm radius. We now consider the possible formation of thicker films on larger droplets. To achieve this, a large aqueous droplet is bombarded for a prolonged period with decane aerosol to increase the volume fraction of decane within the composite droplet. The change in C−H to O−H intensity with time following coagulation is shown in Figure 10a. Two periods of prolonged exposure to decane aerosol are shown prior to 2 and 9 min. During these periods, the C−H intensity grows markedly, dominating the intensity from the O−H Raman band. An inhomogeneous droplet is formed, and the segregation of aqueous and organic phases quenches SRS between 0.5 and 2.5 min and between 8.5 and 11.5 min. Following termination of the decane aerosol flow, the C−H intensity diminishes rapidly due to evaporation on a time scale of ~90 s, after which the SRS surpasses threshold and WGMs reappear in the Raman fingerprint.

After the first coagulation period, layer formation can be inferred from the increase in the first-order mode offset to 5.8 $\pm$ 0.1 nm from 1.3 $\pm$ 0.1 nm before coagulation (shown by black squares in Figure 10a. For droplets larger than 5 μm in radius, the second-order resonances become narrow and their wavelength can be determined accurately. After the first coagulation event, these also display a change in mode offset, although less significant than the first-order modes, increasing from 0.3 $\pm$ 0.1 nm before coagulation to 1.0 $\pm$ 0.1 nm after coagulation. By considering the trends shown in Figure 4, this suggests that the layer formed is less than 400 nm in thickness.

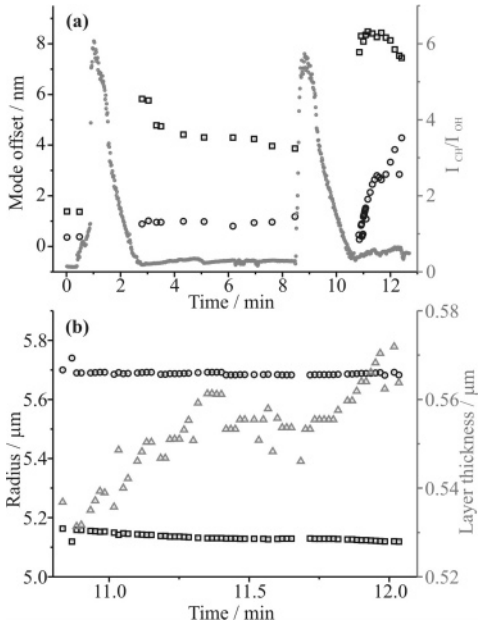

Figure 10. (a) Time dependence of the mode offset for first-order modes (squares, left axis) and second-order modes (open circles, left axis) and the corresponding C−H to O−H band intensity ratio (filled gray circles, right axis) observed following the coagulation of an aqueous sodium chloride droplet with decane droplets at times of around 1 min and 8.5 min. (b) The time dependence of the total (circles, left axis) and core (squares, left axis) radii and the decane layer thickness (gray triangles, right axis).

Following the second coagulation period after 10.5 min, the first-order mode offset remains large with a value between 7.5 and 8.5 nm, while the second-order mode offset increases markedly over the first 90 s following coagulation from ~0.5 to 4 nm. These two changes suggest that a thicker film (~500 nm) is formed and that the decane layer thickness increases with time.

Total and core droplet radii, along with the decane layer thickness, are reported in Figure 10b. The radius of the aqueous core is observed to decrease faster than the outer droplet radius, suggesting that water is evaporating into a gas phase that is rich in decane and depleted in water following the prolonged periods of introduction of decane vapor and aerosol into the tweezing cell. It should be noted that with a core evaporation rate of 0.6 $\pm$ 0.6 nm/s, the mass transfer of water through the decane film remains slower than that through the thinner film described earlier. The evaporation rate of the aqueous core through the decane shell is included in Figure 9b for comparison. In the former case the evaporation rate is 1.0 $\pm$ 0.5 nm/s over the first 5 min, during which time the decane film thickness decreases from 110 to 90 nm. In this thicker shell experiment, the aqueous core size is observed to decrease by ~50 nm, while the decane shell thickens by approximately 40 nm from 530 to 570 nm between 11 and 12 min. Further, the total droplet size decreases marginally by ~20 nm. As the core size decreases in size, an increase in the layer thickness would be anticipated if it is assumed that decane is not evaporating from the surface of the droplet. However, the increase is larger than expected here, and it is assumed that this indicates further partitioning of decane from the gas phase to the droplet.

Throughout this discussion we have interpreted the Raman spectra as being consistent with core−shell structures. This is supported by the quality of the fits obtained when assuming a core−shell structure. We have made no assessment of the uniformity of the decane shell, although it is anticipated that

the shell may not remain uniform in thickness around the entire droplet surface. The slight asymmetry of the resonant modes shown in Figure 1 for the layered droplets may reflect that the organic films are not completely uniform, although the apparent retardation of the water mass transfer rate suggests the film must cover a large fraction of the droplet surface. In future work, we will examine the film uniformity in greater detail.

IV. Conclusions

We have demonstrated that nonlinear Raman spectroscopy can be used to probe the evolution in droplets with a core−shell structure with high time resolution. In these measurements, the unique fingerprint of WGM wavelengths is used to assess the behavior of multiphase decane/aqueous sodium chloride droplets, focusing on the time evolution in the combined droplet structure following coagulation. The aqueous and organic components are immiscible, and discrete phase segregation is observed at early times after coagulation when the volume fractions of the organic and aqueous phases are comparable. At longer times, following evaporation of the organic component, a surface layer is formed with the decane/aqueous phases forming a core−shell structure. All of these observations are consistent with the equilibrium geometries predicted from a consideration of the surface and interfacial tensions.[41,42]

By recording the fingerprint of WGM wavelengths with time, the evolving structure of the droplet can be determined. The aqueous core size can be determined with nanometer accuracy,[18] while the thickness of the organic layer can be determined with an accuracy of ±8 nm. Future work will aim to examine the lower limit on thickness that can be probed.

Changes in evaporation rate for water are observed with change in decane layer thickness, with the organic layer forming a resistive barrier to mass transfer. Future work will explore systematically the dependence of evaporation rate on the thickness of the organic layer and will explore the dependence of the evaporation rate on the solubility and diffusion constant of water in the organic phase. This will require accurate calibration of the gas phase composition, and this will be achieved by trapping a second control homogeneous aqueous droplet beside the core−shell droplet to provide a control measurement.

Acknowledgment. We acknowledge the EPSRC for financial support and for supporting L.M. Dr. Andy Ward is acknowledged for his assistance at the early stages of this work. The Royal Thai government is also acknowledged for studentship support for J.B.

References and Notes

(1) Snead, C. C.; Zung, J. T. *J. Colloid Interface Sci.* **1968**, *27*, 25.
(2) Abbatt, J. P. D.; Broekhuizen, K.; Kumar, P. P. *Atmos. Environ.* **2005**, *39*, 4767.
(3) Andrews, E.; Larson, S. M. *Environ. Sci. Technol.* **1993**, *27*, 857.
(4) Lo, J.-H. A.; Lee, W.-M. G. *Chemosphere* **1996**, *33*, 1391.
(5) Shantz, N. C.; Leaitch, W. R.; Caffrey, P. F. *J. Geophys. Res.* **2003**, *108*, 4168.
(6) Shulman, M. L.; Jacobson, M. C.; Carlson, R. J.; Synovec, R. E.; Young, T. E. *Geophys. Res. Lett.* **1996**, *23*, 277.
(7) Shulman, M. L.; Charlson, R. J.; Davis, E. J. *J. Aerosol Sci.* **1997**, *28*, 737.
(8) Tervahattu, H.; Juhanoja, J.; Kupiainen, K. *J. Geophys. Res.* **2002**, *107*, D164319.
(9) Tervahattu, H.; Hartonen, K.; Kerminen, V.-M.; Kupiainen, K.; Aarnio, P.; Koskentalo, T.; Tuck, A. F.; Vaida, V. *J. Geophys. Res.* **2002**, *107*, D74053.
(10) Tervahattu, H.; Juhanoja, J.; Vaida, V.; Tuck, A. F.; Niemi, J. V.; Kupiainen, K.; Kulmala, M.; Vehkamaki, H. *J. Geophys. Res.* **2005**, *110*, D06207.
(11) Gilman, J. B.; Tervahattu, H.; Vaida, V. *Atmos. Environ.* **2006**, *40*, 6606.
(12) Anttila, T.; Kiendler-Scharr, A.; Tillmann, R.; Mental, T. F. *J. Phys. Chem. A* **2006**, *110*, 10435.
(13) Badger, C. L.; Griffiths, P. T.; George, I.; Abbatt, J. P. D.; Cox, R. A. *J. Phys. Chem. A* **2006**, *110*, 6986.
(14) Rudich, Y. *Chem. Rev.* **2003**, *103*, 5097.
(15) Ellison, G. B.; Tuck, A. F.; Vaida, V. *J. Geophys. Res.* **1999**, *104*, 11633.
(16) Hopkins, R. J.; Mitchem, L.; Ward, A. D.; Reid, J. P. *Phys. Chem. Chem. Phys.* **2004**, *6*, 4924.
(17) Mitchem, L.; Hopkins, R. J.; Buajarern, J.; Ward, A. D.; Reid, J. P. *Chem. Phys. Lett.* **2006**, *432*, 362.
(18) Mitchem, L.; Buajarern, J.; Hopkins, R.; Ward, A. D.; Gilham, R. J. J.; Johnson, R. L.; Reid, J. P. *J. Phys. Chem. A* **2006**, *110*, 8116.
(19) Mitchem, L.; Buajarern, J.; Ward, A. D.; Reid, J. P. *J. Phys. Chem. B* **2006**, *110*, 13700.
(20) Reid, J. P.; Meresman, H.; Mitchem, L.; Symes, R. *Int. Rev. Phys. Chem.* **2006**, *26*, 139.
(21) Reid, J. P.; Mitchem, L. *Annu. Rev. Phys. Chem.* **2006**, *57*, 245.
(22) Carey, D. M.; Korenowski, G. M. *J. Chem. Phys.* **1998**, *108*, 2669.
(23) Starzak, M.; Mathlouthi, M. *Food Chem.* **2003**, *82*, 3.
(24) Li, R.; Jiang, Z.; Chen, F.; Yang, H.; Guan, Y. *J. Mol. Struct.* **2004**, *707*, 83.
(25) Sceats, M. G.; Stavola, M.; Rice, S. A. *J. Chem. Phys.* **1979**, *70*, 3927.
(26) Ray, A. K.; Souyri, A.; Davis, E. J.; Allen, T. M. *Appl. Opt.* **1991**, *30*, 3974.
(27) Aden, A. L.; Kerker, M. *J. Appl. Phys.* **1951**, *22*, 1242.
(28) Toon, O. B.; Ackerman, T. P. *Appl. Opt.* **1981**, *20*, 3657.
(29) Huckaby, J. L.; Ray, A. K.; Das, B. *Appl. Opt.* **1994**, *33*, 7112.
(30) Ray, A. K.; Devakottai, B.; Souyri, A.; Huckaby, J. L. *Langmuir* **1991**, *7*, 525.
(31) Wiscombe, W. J. Calculation of Light Scattering by Coated Spheres, ~ftp://climate.gsfc.nasa.gov/pub/wiscombe/Single-Scatt/Coated-Sphere/ 1993.
(32) *Handbook of chemistry and physics*, 87th ed.; CRC Press: Boca Raton, FL, 2006−2007.
(33) Buajarern, J.; Mitchem, L.; Ward, A. D.; Nahler, N. H.; McGloin, D.; Reid, J. P. *J. Chem. Phys.* **2006**, *125*, 114506.
(34) Symes, R.; Sayer, R. M.; Reid, J. P. *Phys. Chem. Chem. Phys.* **2004**, *6*, 474.
(35) Economou, I. G.; Heidman, J. L.; Tsonopoulos, C.; Wilson, G. M. *AIChE J.* **1997**, *43*, 535.
(36) Galleguillos, R. R.; Taboada, M. E.; Graber, T. A.; Bolado, S. *J. Chem. Eng. Data* **2003**, *48*, 405.
(37) Butler, J. R.; Mitchem, L.; Hanford, K. L.; Treuel, L.; Reid, J. P. *Faraday Discuss.* **2007**, *137*, In press.
(38) Wyslouzil, B. E.; Wilemski, G.; Strey, R.; Heath, C. H.; Dieregsweiler, U. *Phys. Chem. Chem. Phys.* **2006**, *8*, 54.
(39) Snow, J. B.; Qian, S.-X.; Chang, R. K. *Opt. Lett.* **1985**, *10*, 37.
(40) Lee, B.-W.; Kwon, M.-Y.; Kim, J.-J. *Chin. J. Phys.* **1990**, *28*, 1.
(41) Torza, S.; Mason, S. G. *J. Colloid Interface Sci.* **1970**, *33*, 67.
(42) Buajarern, J.; Mitchem, L.; Reid, J. P. *J. Phys. Chem. A* **2007**. In press.